

CaCO₃ Nanoparticles Coated with Alternating Layers of Poly-L-Arginine Hydrochloride and Fe₃O₄ Nanoparticles as Navigable Drug Carriers and Hyperthermia Agents

Evgeny S. Vavaev, Marina Novoselova, Nikita M. Shchelkunov, Sergei German, Aleksei S. Komlev, Maksim D. Mokrousov, Ivan V. Zelepukin, Andrey M. Burov, Boris N. Khlebtsov, Evgeny V. Lyubin, Sergey Deyev, Andrey A. Fedyanin, and Dmitry A. Gorin*



Cite This: *ACS Appl. Nano Mater.* 2022, 5, 2994–3006



Read Online

ACCESS |



Metrics & More



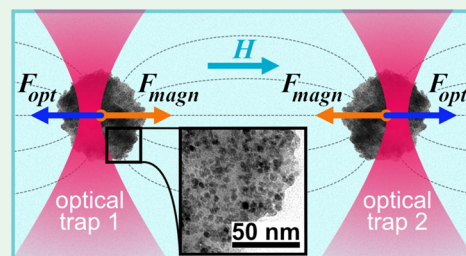
Article Recommendations



Supporting Information

ABSTRACT: Nanocomposite capsules containing magnetite nanoparticles (MNPs) are promising multifunctional drug delivery systems for various biomedical applications. The presence of MNPs allows one to visualize these capsules via magnetic resonance imaging (MRI) and optoacoustic (photoacoustic) imaging. Moreover, we can ensure precise navigation and remote release via a magnetic field gradient and alternating magnetic fields, respectively. Magnetic dipole–dipole interaction between single capsules is important when a magnetic field is applied, and it is determined by a magnetic moment of each individual capsule. However, there is a lack of experimental data on the magnetic moment of a single capsule. Physical properties of capsules vary due to the change in the volume fraction of MNPs, as well as the capsule shell architecture. Therefore, two types of submicron capsules with different amounts of MNPs were synthesized. The first type of capsules was prepared by freezing-induced loading and layer-by-layer (LbL) assembly. The amount of MNPs varied by the number of freezing-induced loading cycles: two, four, and six. The second type of capsules is a nanocomposite shell formed using the LbL assembly of the oppositely charged polyelectrolytes and MNPs. Structural properties of both types of submicron capsules and MNPs were studied using transmission electron microscopy. Magnetic moments of nanocomposite shells placed in an external magnetic field were directly measured by optical tweezers and calculated based on vibrating-sample magnetometer measurements of the water suspension of nanocomposite shells. The magnetic moment of an individual shell depends on the amount of MNPs and increases as the number of MNPs per shell grows. Magnetic coupling parameters and the specific absorption rate were calculated. The obtained results can be applied while preparing drug carrier systems sensitive to alternating magnetic fields and navigated by gradient magnetic fields. They can also be taken into account in device development for navigating drug delivery systems and for the treatment based on alternating magnetic field-induced hyperthermia.

KEYWORDS: magnetic moment of a single capsule, shell, magnetite nanoparticles, layer-by-layer assembly, freezing-induced loading, optical tweezers, specific absorption rate, vibrating-sample magnetometer magnetic measurements



1. INTRODUCTION

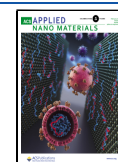
Harnessing nanoparticles in drug delivery has been considered as a promising approach in various biomedical applications. However, the delivery of drugs through nanoparticles has been recently critically overviewed showing that the main challenge in this field is the low delivery efficiency. Wilhelm et al. demonstrated that only 0.7% of the administered nanoparticles are delivered to solid tumors.¹ This study shows that chemical addressing by the surface modification of drug delivery systems using molecules with specific adhesion to the targeted cells increases the delivery efficiency from 0.6% for passive addressing to 0.9% for the active one.¹ The alternative approach is physical addressing by optical,² acoustic,³ and magnetic⁴ tweezers. A comparative analysis of these methods mentioned above is present in the work of Ozelik et al.⁵ The magnetic tweezers technique provides remote navigation of

drug delivery systems using magnetic field gradients for nanocomposite capsules,⁴ magnetotactic bacteria,⁶ and micro-propellers.⁷ Moreover, a promising task is the development of multifunctional drug delivery systems that combine many functions such as visualization, remote release, and navigation.⁸ Imaging techniques include fluorescence molecular tomography,⁸ magnetic resonance imaging (MRI),⁸ optical coherence tomography,⁹ and the new ones such as optoacoustic microscopy⁸ and tomography.¹⁰ Many approaches have

Received: January 21, 2022

Accepted: February 1, 2022

Published: February 11, 2022



already been used for the remote release of encapsulated drugs, including laser irradiation,¹¹ alternating magnetic fields,^{12,13} and ultrasound¹⁴ including high-intensity focused ultrasound.⁸ Precise navigation can be implemented via optical² and acoustic tweezers⁵ and the magnetic field gradient.⁴ Currently, only magnetic field gradient approaches have been applied in vivo.⁴ The navigation of multifunctional drug carrier systems is realized by nanocomposite carriers containing large amounts of magnetite nanoparticles (MNPs).⁸ Various types of nanocomposite objects have been prepared including core-shell particles,¹⁵ a nanocomposite shell,¹⁵ a lipid/polymer shell with encapsulated MNPs,^{8,16} gas bubbles stabilized by dye-surfactant complexes,¹⁷ or nanoparticles with the polymer shell.¹⁷

There are several MNP synthesis methods, one of them is thermal decomposition, but it requires precursors that have toxic effects.¹⁸ In this study, we aim for the biomedical application, and therefore, we try to avoid toxicity and use simple and cheap synthesis that also could be carried out under sterile conditions in a chemical reactor. As a result, we realized Massart's precipitation method with modifications.¹⁹ The peculiarity of all precipitation methods is that it is hard to obtain the uniform distribution of the resulting nanoparticles. The difference of MNPs in size is not dramatic and is acceptable for our applications.

Doxorubicin (DOX) is one of the well-known anthracycline antibiotics and is widely used as an antitumor chemotherapy medication.²⁰ The main advantage of this drug is that it is fluorescent and the peaks of emission (560 and 590 nm)²¹ are in the optical transparency window of the biological tissue, that is why DOX can be used for biodistribution studies. The crucial factor limiting the use of DOX is its extremely high cardiotoxicity. Therefore, it is important to develop methods of targeted delivery of DOX that could reduce its side effects on the cardiovascular system. As in a previous work, drug delivery carriers DOX with MNP were visualized with several methods such as MRI and fluorescence tomography and optoacoustics.⁸ Moreover, the ability for the remote release of encapsulated DOX by focused ultrasound has been shown.⁸ In this study, DOX was used as a model therapeutic agent.

There are efficient approaches to prepare drug delivery carriers loaded by different types of cargo including layer-by-layer (LbL) assembly,^{22,23} freezing-induced loading (FIL),¹⁵ and their combinations.¹⁰ LbL assembly has already been used for preparing nanocomposite films and shells containing MNPs^{4,24} and polymer shells for the encapsulation of MNPs embedded in vaterite particles using FIL.⁸ The nanocomposite shells with encapsulated MNPs have also been prepared using LbL²⁵ and FIL methods,⁸ and their characteristics were explored through MRI.^{8,25,26} Core-shell particles are given particular attention in biomedicine and pharmacology.^{27,28} Magnetic nanoparticles embedded in microcapsules make them controllable, thus providing for an enhanced efficiency of drug delivery carrier systems.^{29,30}

The behavior of particles containing MNPs under a magnetic field gradient was recently considered.³¹ There are two types of particle movement under the impact of the magnetic field gradient – magnetophoresis: cooperative magnetophoresis and magnetophoresis-induced convection.³¹ Cooperative magnetophoresis is a collective motion of strongly interacting particles. The gradient field is created because of the appearance of a local magnetic field in each of the particles magnetized in the same direction. The convection type is

induced by an external inhomogeneous magnetic field³¹ and can be calculated using the magnetic dipole moment of each individual particle. Parameters of aggregation and magnetic coupling can be used for determining the type of particle behavior in the magnetic field. Because of the stable structure and the ability to control the position and filler release by means of a magnetic field, these types of particles help deliver a drug to the target organ or part of the body. When working with such agents, it is important to precisely determine their mechanical and magnetic properties that govern their behavior and movement in biological tissues and organisms.

Knowledge of the magnetic moment of nanocomposite drug carriers allows us to predict the behavior of such objects in vivo. Preclinical studies use nanocomposite carriers at concentrations of 10^8 – 10^9 mL⁻¹ and volume of injections using magnetic suspensions amounting to 10–100 μ L.

The properties of magnetic suspensions are usually studied via the dynamic light scattering (DLS) method or other scattering techniques^{32,33} and vibrating-sample magnetometry.^{34,35} However, these approaches characterize the suspension in general, still providing little information about individual particles. Moreover, the measurements of magnetic properties are often carried out for a dried or very concentrated suspension, and mutual magnetization of micro-particles strongly affects the obtained results.

Optical tweezers are a unique experimental technique that allows for studying the properties of a single submicron object and measuring the forces acting in microsystems with greater precision.^{2,36–38} It had previously been shown that the magnetic interaction forces of microparticles could be measured with an accuracy of 1 fN and the magnetic moment of an individual microparticle with an accuracy of about 10^{-16} A·m² using this technique,^{39,40} which makes optical tweezers a promising method for characterizing individual magnetic microcapsules.

The ability of nanoparticles to heat in an alternating magnetic field is their crucial feature used for inducing local heating in tumors. The specific absorption rate (SAR) is a parameter that characterizes the heating power of a substance at the fixed values of intensity and frequency of the alternating magnetic field. The SAR value varies widely for different materials from 0.35 to 6000 W/g.^{41,42} The most promising materials that can be used in designing the practice are nanoparticles of ferrite,^{43,44} manganite,^{45,46} and gadolinium-based alloys.^{47,48} Heating of ferromagnetic particles occurs due to two mechanisms: the Néel relaxation of magnetization (hysteresis process) and the mechanical rotation of the particles. Consequently, the magnetic properties of particles, their size, architecture, and viscosity of the medium are the key parameters determining the SAR value.

The presence of MNPs allows for achieving the multifunctionality of nanocomposite carriers: besides the ability of their targeted delivery by the application of a magnetic field gradient,⁴⁹ the carriers could be visualized by MRI;⁸ the inclusion of MNPs gives the opportunity of local heating target area by alternating magnetic field⁵⁰ and remote release of encapsulated substances.⁵¹

Therefore, measurements of the magnetic moment of an individual nanocomposite carrier prepared using LbL or a combination of LbL and FIL is an actual task for practical applications in modern biophysics and interface science. This study provides new knowledge on the effect of the FIL cycle number and the MNP volume fraction on the magnetic

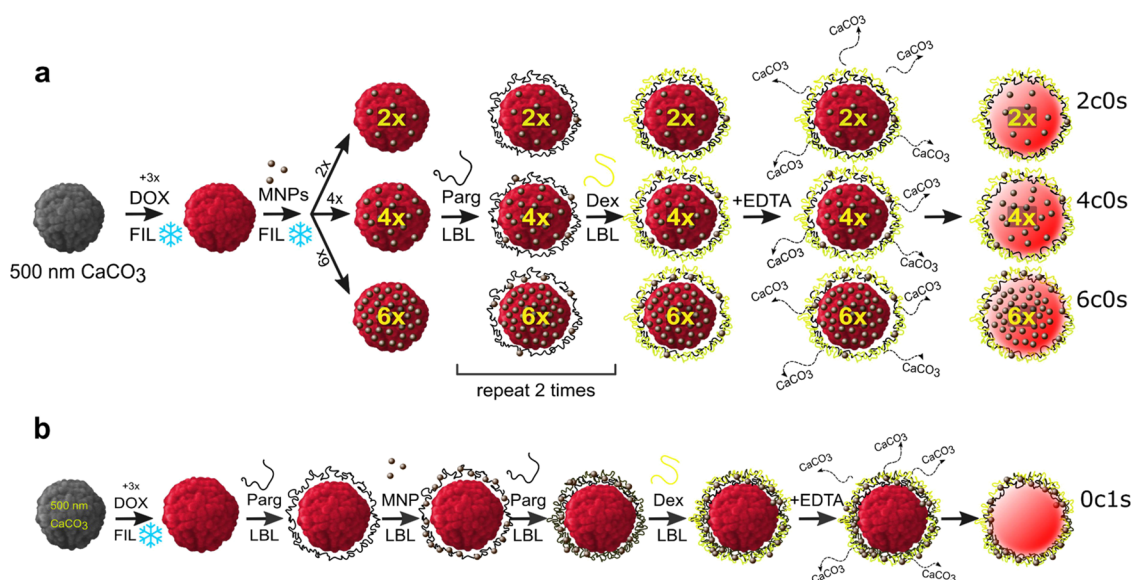


Figure 1. Schemes of sample preparation with MNP loading to (a) core: 2c0s, 4c0s, and 6c0s and (b) shell: 0c1s (sample notation: XcYs, where X is the number of FIL loadings per core, Y is the number of magnetite nanoparticle layers formed using the LbL method).

moment of individual capsules obtained using the optical tweezers technique. The obtained data are compared with vibrating-sample magnetometry. Several important parameters determining the behavior of nanocomposite carriers under the impact of the magnetic field gradient and the alternating magnetic field are numerically obtained.

2. EXPERIMENTAL SECTION

2.1. Materials. Poly-L-arginine hydrochloride (Parg, $M_w = 15\text{--}70$ kDa), dextran sulfate sodium salt (Dex, $M_w = 100$ kDa), glycerol, phosphate buffer solution (PBS), sodium hydroxide (99.8%), iron(III) chloride hexahydrate ($\text{FeCl}_3 \cdot 6\text{H}_2\text{O}$), iron(II) chloride tetrahydrate ($\text{FeCl}_2 \cdot 4\text{H}_2\text{O}$), ethylenediaminetetraacetic acid disodium salt (EDTA), hydrochloric acid, calcium chloride dihydrate, anhydrous sodium carbonate, sodium chloride, and sodium hydroxide were purchased from Sigma-Aldrich (USA); doxorubicin (DOX) (“Omutninsk Scientific Experimental Industrial Base,” Russia). Deionized (DI) water with specific resistivity higher than $18.2 \text{ M}\Omega \cdot \text{cm}$ from Milli-Q Plus 185 (Millipore) water purification system was used to make all solutions.

2.2. Methods. **2.2.1. Synthesis of MNPs.** MNPs were obtained by chemical precipitation from salts of di- and trivalent iron in the presence of a base. Initially, 0.65 g of $\text{FeCl}_3 \cdot 6\text{H}_2\text{O}$ and 0.24 g of $\text{FeCl}_2 \cdot 4\text{H}_2\text{O}$ were dissolved in water at room temperature with mixing. Then, 100 mL of 0.1 M NaOH was added to the reaction cell. For further colloid stabilization, 25 mL of citric acid (16 mg/mL) solution was prepared. To remove oxygen from iron salts, the stabilizing agent, and sodium hydroxide solution, nitrogen was bubbled across the closed cells with mixing for 10 min. After that, iron salt solutions were injected into the sodium hydroxide solution for over several seconds with active mixing, followed by active mixing of the solution for 4 min. Then, 25 mL of citric acid (20 mg/mL) was added to the suspension with constant mixing. The synthesis of MNPs and their coating with citric acid were carried out in the nitrogen atmosphere using the chemical reactor TetraQuant CR-1 (TetraQuant LLC, Russia). The dialysis of magnetic hydrosol was conducted for four days in a 1.2 L vial with slow mixing. Mixing of the reagents and the washing steps were carried out in the nitrogen atmosphere.

2.2.2. Preparation of Nanocomposite Microcapsules. Submicron-sized CaCO_3 templates (~ 500 nm in diameter on average) were synthesized as described elsewhere.⁵² In brief, 4 g of glycerol was mixed with aqueous solutions (0.4 mL of CaCl_2 and 0.4 mL of Na_2CO_3) in equal concentrations (0.5 M) with vigorous stirring at

700 rpm at room temperature. After 1 h of continuous stirring, the suspension was centrifuged, and the precipitate was washed with excess DI water five times to remove glycerol.

The schemes for capsule preparation are shown in Figure 1. Loading of the template with DOX for all types was performed using the FIL method¹⁵ with a mini-rotating device TetraQuant R-1 (TetraQuant LLC, Russia) in a single loading cycle. The loaded particles were separated by centrifugation at 8000 rpm for 1 min. The supernatant was then analyzed to determine the drug content.

The sample notation has the form XcYs, where X is the number of FIL loadings per core, and Y is the number of magnetite nanoparticle layers formed using the LbL assembly method. Samples 2c0s, 4c0s, and 6c0s were assembled on the CaCO_3 template with DOX by sequential (one to six times) loading of MNPs using the FIL method¹⁵ (Figure 1a). Then, the shell was formed by the adsorption of 1 mL of the oppositely charged Parg (0.5 mg/mL in 0.15 M NaCl) and Dex (1 mg/mL in 0.15 M NaCl) by the spherical surface of calcium carbonate cores with DOX and MNPs. After adsorption, the cores were dissolved by treatment with EDTA sodium salt solution (concentration in water, 0.2 M). After each adsorption step as well as after dissolving calcium carbonate cores, the suspension of the capsules was centrifuged and washed two times with pure water. The capsules 0c1s were assembled on the obtained template with DOX by sequential alternate adsorption (using the LbL technique) of Parg, MNPs, and Dex (Figure 1b).

CaCO_3 template loadings were conducted in the following way. Vaterite particle suspension was added to the DOX solution in the polymeric tube and then frozen under mixing according to the FIL method. After the mixture was completely frozen, it was thawed and washed two times with DI water. Then, this freezing–thawing cycle was repeated two times (the first step in Figure 1a, b). The template particles for samples 2c0s, 4c0s, and 6c0s were prepared by the loading of MNPs after DOX was loaded. The loading was done in a similar way by adding vaterite particles loaded with DOX to the MNP suspension in the polymeric tube and then conducting freezing–thawing cycles (the second step in Figure 1a). For samples 2c0s, 4c0s, and 6c0s, the freezing–thawing cycles were repeated 2, 4, and 6 times, respectively, as denoted above.

The shell of the samples was obtained using the LbL assembly method, which is sequential adsorption of oppositely charged materials onto a substrate. The template particles were added in the Parg solution in the polymeric tube, and then, the suspension was stirred for 15 min on the shaker. When the stirring was done, the mixture was centrifuged and washed three times with DI water

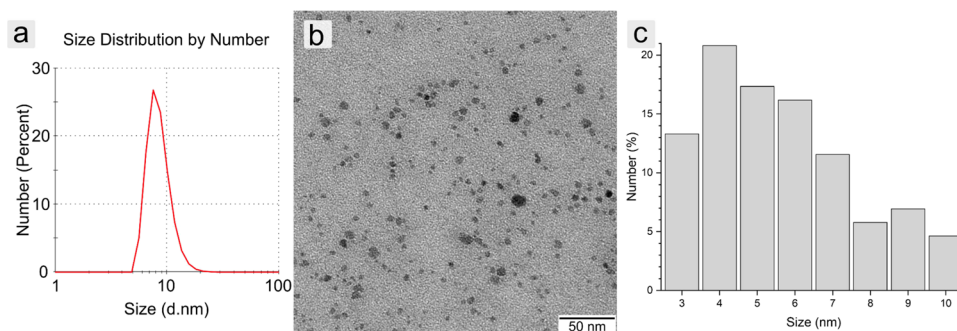


Figure 2. Magnetite nanoparticle size distribution by DLS measurements (a), TEM image (b), and nanoparticle size distribution by TEM analysis (c).

(Figure 1a, step 3). After that, the particles were ready for the next layer deposition, which was done in a similar way, but Parg was changed with Dex (Figure 1a, step 4). The deposition of these two layers was repeated one more time, and in the result, we obtained the shell with the structure of type Parg/Dex/Parg/Dex.

The templates for sample 0c1s after loading with DOX three times were added in the Parg solution in the polymeric tube and then stirred as described earlier (step 2 in Figure 1b). The next layer was adsorbed in a similar way, but Parg was changed to MNPs (step 3 in Figure 1b). The last two layers of Parg and Dex were deposited in the same way as for samples 2c0s, 4c0s, and 6c0s (Figure 1a), and the resulting shell structure of 0c1s is Parg/MNP/Parg/Dex (Figure 1b).

Each polymer was used as a 1 mg/mL aqueous solution with 0.15 M NaCl. CaCO_3 cores were dissolved by treatment with 0.2 M EDTA. After each adsorption step and the EDTA treatment, we washed the microparticles with DI water twice. As a result, two types of samples were obtained: 2c0s, 4c0s, and 6c0s with different amounts of MNPs in the core (Figure 1a) and 0c1s (Figure 1b).

2.2.3. Characterizing the Particles and Capsules. Concentrations of magnetite in all samples were measured through the colorimetric titration method based on the qualitative reaction of Fe^{3+} ions with ammonium thiocyanate. First, the magnetite colloid/core-shell suspension was dissolved in 1 M H_2SO_4 solution for 24 h. Second, 100 μL of the dissolved suspension was diluted by 800 μL of water. Then, 100 μL of 4 M water solution of ammonium thiocyanate was added to the sample, and absorption at a wavelength of 473 nm was measured. Absorption of the standard Fe^{3+} solution in 1 M H_2SO_4 with the known concentration was used to obtain a calibration curve. The amount of magnetite in the solution was calculated using the calibration curve.

For iron quantification, inductively coupled plasma mass spectrometry (ICP-MS) was used. The capsules with magnetic nanoparticles were dissolved in concentrated nitric acid during incubation at 60 $^\circ\text{C}$ for 2 h. Then, solutions were 10-fold diluted with distilled water, and the Fe concentration was measured using a NexION 2000 mass spectrometer (Perkin Elmer, USA). The device was calibrated using serial dilutions of FeCl_3 salt.⁵⁷ The Fe peak was used for analysis. The ICP-MS measurements of the sample with the maximum MNP loading are 0.780 ± 0.049 g/L, which is in a good correlation with the 0.610 ± 0.007 g/L value obtained using the titration method.

The particle morphology and elemental composition were characterized by scanning electron microscopy (SEM) with an MAIA3 (Tescan, Czech Republic) microscope coupled with an energy dispersive spectrometry (EDS) detector (X-act, Oxford Instruments, High Wycombe, UK). Nanoparticles in water were dropped on the silicon grid and dried under the air. Electron micrographs were obtained at an accelerating voltage of 20 kV using the secondary electron detection mode.

The determination of the size of the particles and the appearance of the synthesized capsules were carried out using transmission electron microscopy (TEM) (Libra 120, Carl Zeiss, Germany; 120 kV).

The average size of MNPs measured using the DLS method (Zetasizer Nano ZS, Malvern, UK) was 9 ± 3 nm (Figure 2a). This result was confirmed by TEM images (6 ± 2 nm) (Figure 2b). The concentration of the magnetite colloid was 0.626 mg/mL.

The magnetic properties of samples were measured using dual-trap optical tweezers combined with four electromagnets. The experimental setup of optical tweezers is shown in Figure 3. The setup

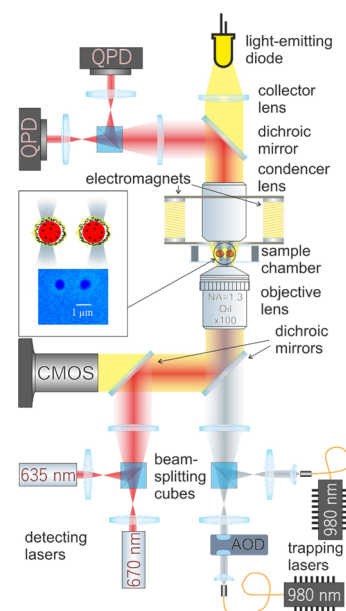


Figure 3. Experimental setup of optical tweezers for studying the magnetic properties of microcapsules. The inset shows a micrograph of two capsules (2c0s) in optical traps.

included two single-mode infrared lasers with a wavelength of 980 nm. Two optical traps were formed by strongly focusing laser beams on a sample chamber using an oil immersion objective lens with a numerical aperture of 1.3 and a working distance of 0.2 mm. The objective lens was mounted on the focusing system. The chamber with a sample was located on a two-coordinate mechanical stage. An acousto-optical deflector (AOD) was used for precise positioning of one of the traps. The experimental setup was equipped with two additional lasers with output wavelengths of 635 and 670 nm and a power of 0.3 mW each, which were used to detect the displacement of the trapped objects by the registration of laser radiation scattered on the trapped particles using two-quadrant photodiodes (QPDs). To visualize the trapped objects, light from the light-emitting diode (LED) passed through the sample and was collected by the objective on a complementary metal-oxide-semiconductor video camera. Four electromagnets were located around the sample and provided a uniform alternating magnetic field up to 62 Oe in the area of the

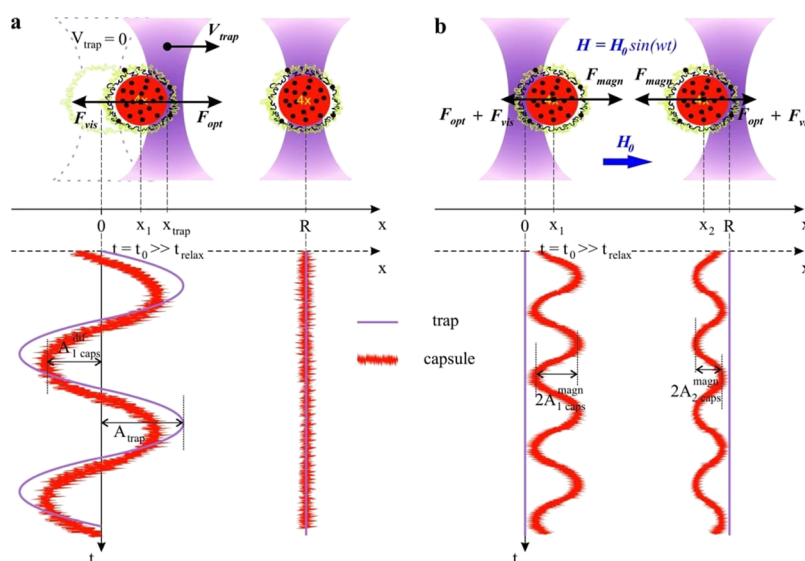


Figure 4. Scheme of optical trapping for two magnetic capsules: (a) position of one of the traps oscillates; (b) an external alternating magnetic field is applied.

trapped objects. For more information about the optical tweezers setup⁵³ and the electromagnet system,⁵⁴ see the previously published articles.

2.3. Optical Tweezers Measurements. Coverslips were treated with 3% hydrogen peroxide. Then, 45 μL of the capsule suspension was placed between two coverslips and sealed using an adhesive tape and soft paraffin. The chamber with the sample prepared in this way was placed on the stage of optical tweezers.

Two capsules were trapped by optical tweezers at a distance of 10 μm above the cover glass of the chamber and photographed to determine their size and distance between them. A typical micrograph of the trapped capsules is shown in the inset of Figure 3. The optical power of laser radiation in the beam waist was 6 mW for each trap.

In the first measurement (Figure 4a), the position of one of the traps was oscillated sinusoidally with a frequency of $\nu = 8$ Hz and an amplitude of $A_{\text{trap}} = 105$ nm in the observation plane using AOD. Time dependence of the signal from QPD was recorded for 50 s, making it possible to determine the amplitude of capsule oscillations, which was smaller than the trap oscillation amplitude.

Neglecting the contribution of Brownian motion and a fictitious force, the motion of the capsule in the oscillating trap is described by the following equation:

$$\gamma x' + kx = kA_{\text{trap}} \sin(2\pi\nu t) \quad (1)$$

where x is the capsule coordinate, γ is the coefficient of viscous friction determined by Stokes' law, and k is the effective trap stiffness. The solution of eq 1 is sought in the form of forced oscillations $x(t) = \text{Im}(\hat{x}e^{i2\pi\nu t})$, where \hat{x} is the complex amplitude of the capsule oscillations and provides the expression for the amplitude of capsule oscillations:

$$A_{\text{caps}}^{\text{dif}} = \frac{kA_{\text{trap}}}{\sqrt{k^2 + 4\pi^2\gamma^2\nu^2}} \quad (2)$$

The derivation of eq 2 is given in eqs S1–S9.

In the second measurement, trajectories of the capsule motion were recorded for 50 s, while both traps were static, and the electromagnets created a uniform alternating magnetic field with a frequency of $\nu/2 = 4$ Hz and an amplitude of $H_0 = 62$ Oe in the area where the trapped capsules were located (Figure 4b). The vector of the magnetic field strength was directed along the line connecting the centers of the optical traps. The field periodically induced magnetic moments in the capsules and caused the oscillating force of mutual magnetic attraction. Under the impact of the force, the capsules were periodically displaced from the centers of the optical traps with an

amplitude $A_{\text{caps}}^{\text{magn}}$ at the doubled frequency of magnetic field oscillations, which corresponds to the following equation of motion:

$$\gamma x' + kx = F_{\text{magn}} \sin^2(\pi\nu t) \quad (3)$$

In the approximation of magnetic dipole interaction of capsules, the amplitude of the attraction force is given as follows:

$$F_{\text{magn}} = \frac{3\mu_0\alpha^2H_0^2}{2\pi R^4} \quad (4)$$

where α is the effective magnetic susceptibility of the capsule, and $\mu_0 = 4\pi \times 10^{-7} \text{ N} \cdot \text{A}^{-2}$ is the magnetic permeability of free space. The solution of the equation of motion is sought in the form of forced oscillations $x(t) = \text{Re}(\hat{x}e^{i2\pi\nu t})$ and provides the following expression for the amplitude of capsule oscillations caused by magnetic interaction:

$$A_{\text{caps}}^{\text{magn}} = \frac{F_{\text{magn}}}{2\sqrt{k^2 + 4\pi^2\gamma^2\nu^2}} \quad (5)$$

The derivation of this equation is given in eqs S10–S17. A typical value of $A_{\text{caps}}^{\text{magn}}$ is 2.5 nm.

In the third measurement, the magnetic field was turned off, and the Brownian motion of the capsules in static traps was recorded for 50 s. The effective stiffness of the optical trap k was determined using the protocol of the previously published work.⁴⁰ All measurements were carried out at a temperature of 22 $^\circ\text{C}$.

Finally, the amplitudes of the magnetic interaction force F_{magn} and the magnetic moment m_{OT} are determined as follows:

$$F_{\text{magn}} = 2 \frac{A_{\text{caps}}^{\text{magn}}}{A_{\text{caps}}^{\text{dif}}} kA_{\text{trap}} \quad (6)$$

$$m_{\text{OT}} = \sqrt{\frac{2\pi R^4 F_{\text{magn}}}{3\mu_0}} \quad (7)$$

The derivation of eq 6 is given in supplementary materials.

2.4. Vibrating-Sample Magnetometer Measurements. Hysteresis loops of the samples were obtained using a vibrating-sample magnetometer (VSM) LakeShore 7407 Series. Measurements of the magnetic properties of the particles were carried out in a liquid medium. The sample was poured into a capillary tube with a volume of 15 μL ; then, the ends of the capillary tube were sealed with paraffin wax. Because the samples had small magnetic moment values, the

diamagnetic signals from the holder and the capillary tube were crucial. Additional subtraction of the result obtained for an empty container from the hysteresis loop increased the reliability of the final data. The magnetic moment per particle was calculated using data on the particle concentration in a liquid. This technique for determining the magnetic moment of bulk samples allowed us to confirm the results obtained using the dual-trap optical tweezers. In addition, the value of magnetic susceptibility, which was determined based on hysteresis loops, is used in further theoretical calculations of the SAR parameter.

2.5. Calculation of Sample Parameters. The mean interparticle distance (MIPD) is proportional to the volume or area per particle. For samples with MNPs dispersed in the core, eq 8 was used:

$$\langle r \rangle_v = \frac{1}{\sqrt[3]{\frac{N}{V}}} \quad (8)$$

where N is the number of MNPs in an individual capsule, V is the volume of the capsule, and r is MIPD. For samples with MNPs dispersed in the shell, we used the following equation:

$$\langle r \rangle_s = \frac{1}{\sqrt[2]{\frac{N}{S}}} \quad (9)$$

where N is the number of MNPs in a capsule shell, S is the surface area of the capsule, and r is MIPD.

Aggregation parameter N^* was calculated using the following equation:³¹

$$N^* = \sqrt{\phi_0 e^{(\Gamma-1)}} \quad (10)$$

where ϕ_0 is the volume fraction of magnetic particles in the solution, which can be easily computed based on its mass concentration. Γ is the magnetic coupling parameter,³¹ which is the ratio between the magnetic energy of two magnetized capsules in contact and thermal energy:

$$\Gamma = \frac{\mu_0 m_{OT}^2}{2\pi d^3 k_B T} \quad (11)$$

where m_{OT} is the magnetic moment of the capsule measured by optical tweezers; d is the average diameter of the capsule; k_B is the Boltzmann constant, and T is the absolute temperature.

SAR is calculated by dividing the heating power of the particles by their unit mass of magnetic particles:

$$SAR = \frac{1}{\phi \rho} \pi \mu_0 f H_0^2 \chi_0 \frac{2\pi f \tau}{1 + (2\pi f \tau)^2} \quad (12)$$

where ρ is the material density of magnetic particles, ϕ is the volume fraction of magnetic particles in the fluid, μ_0 is the magnetic constant, f is the frequency of the external alternating magnetic field, H_0 is the external alternating magnetic field amplitude, χ_0 is the static magnetic susceptibility, and τ is the effective relaxation time of the system. The most significant contribution to the caloric properties, which determines the value of SAR, is made by the relaxation time τ of the rotation frequency of the magnetic moment. The rotation of the magnetic moment in an alternating magnetic field occurs under the action of two mechanisms: the Néel mechanism of rotation of the magnetic moment and the Brownian rotation of the particle.

$$\tau = \frac{\tau_B \times \tau_N}{\tau_N + \tau_B} \quad (13)$$

The Néel relaxation time τ_N and the Brownian rotational relaxation time τ_B of the particle are given as follows:

$$\tau_N = \frac{\sqrt{\pi}}{2} \tau_0 \frac{e^{KV/kT}}{\sqrt{\frac{KV}{kT}}} \quad (14)$$

$$\tau_B = \frac{3\eta V_H}{kT} \quad (15)$$

where η is the dynamic viscosity coefficient, V_H is the hydrodynamic volume of a particle, and K is the magnetic anisotropy constant.

The magnetophoretic velocities were also calculated for all samples. Submicron capsules moving through the bloodstream in a vessel in the presence of an external inhomogeneous magnetic field experience various external forces. The capsules are acted upon by the force of viscous friction, the force of Brownian motion, the buoyancy force from the liquid medium they move in, and by a magnetophoretic force from an external magnetic field. There are also the inertia forces, the gravity force, and the force of particle-particle hydrodynamic and magnetic interactions. However, all these forces for capsules with a diameter of less than 1 μm are negligible in comparison with the magnetophoretic force and the force of viscous friction and therefore may not be taken into account.^{55,56} Thus, only two forces make the main contribution to the right side of the motion equation of the capsules in the bloodstream: the force of viscous friction and the magnetophoretic force.

Considering the blood to be a Newtonian fluid with dynamic viscosity $\eta_b = 4.5 \text{ mPa}\cdot\text{s}$ at 37 $^\circ\text{C}$,⁵⁶ the viscous friction force is determined using Stoke's law:

$$\mathbf{F}_D = -6\pi\eta_b r \mathbf{v} \quad (16)$$

where r is the hydrodynamic radius that coincides with the radius of the capsule, and \mathbf{v} is the capsule velocity relative to the blood. Vector quantities are indicated in bold.

The magnetophoretic force acting on the capsules in the dipole approximation can be written as follows:

$$\mathbf{F}_M = \nabla(\mathbf{m}\mathbf{B}) \quad (17a)$$

where \mathbf{m} is the capsule magnetic moment and \mathbf{B} is the external magnetic flux density. Considering the saturation fields and assuming that the capsule magnetic moment is always directed along the external magnetic field, eq 17a can be rewritten passing from vectors to their absolute values and removing the magnetic moment from the action of the nabla operator:

$$\mathbf{F}_M = m_s \nabla B \quad (17b)$$

where $m_s = |\mathbf{m}_s|$ is the capsule magnetic moment in saturation, $B = |\mathbf{B}|$, and ∇B is the magnetic flux density gradient at the point of the capsule location.

Considering that the mass of the capsule is small, the equation of capsule motion in the bloodstream takes the following form:

$$\mathbf{F}_D + \mathbf{F}_M = 0 \quad (18)$$

Eq 18 allows one to determine the capsule magnetophoretic velocity caused by the gradient of the external magnetic field:

$$\mathbf{v} = \frac{m_s \nabla B}{6\pi\eta_b r} \quad (19)$$

3. RESULTS AND DISCUSSION

LbL assembly and its combination with the FIL method were successfully applied for preparing two types of capsules with MNPs. The average size of the nanoparticles measured using the DLS method is $9 \pm 3 \text{ nm}$ (Figure 2a). The TEM image of MNPs is presented in Figure 2b. The average size of $6 \pm 2 \text{ nm}$ obtained from the TEM images is consistent with the values measured using the DLS method.

The first type of capsules with different amounts of MNPs was prepared using FIL and LbL assembly. Two, four, and six FIL cycles of MNPs were carried out to vary the amount of nanoparticles dispersed inside the polymer shells.

The second type of capsules is a typical example of a nanocomposite shell produced using LbL. A similar approach

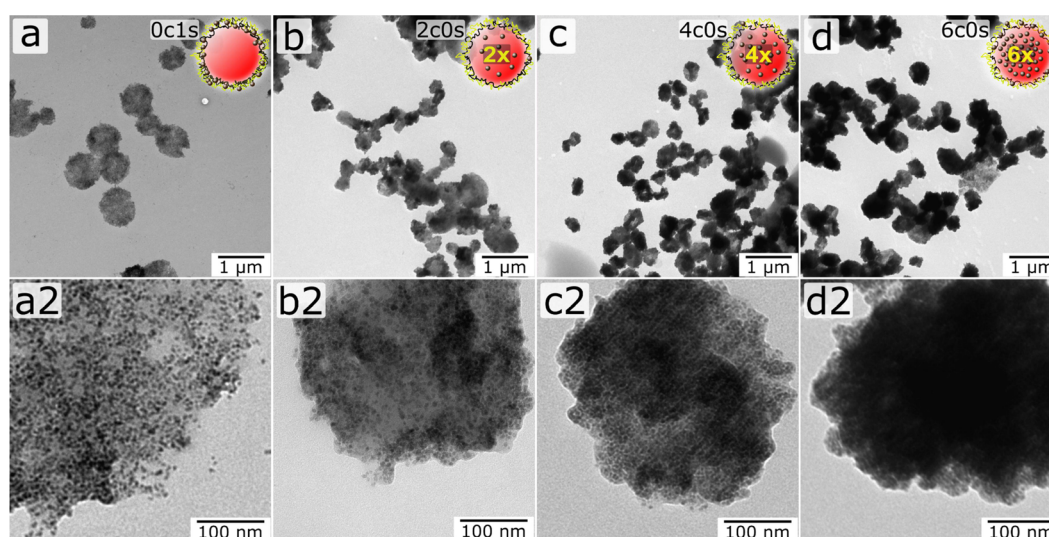


Figure 5. TEM images of the samples with MNPs embedded inside the shell using the LbL method, 0c1s (a, a2), and within the inner volume of capsules with a different number of MNP loading by FIL – 2 – 2c0s (b, b2), 4 – 4c0s (c, c2), 6 – 6c0s (d, d2), respectively.

is described in previous studies.^{4,9,11,24,25} The difference consists in the submicron size of the shell as well as in vaterite particles that were used as templates.

Both types of microcapsules were characterized by TEM (Figure 5). TEM images show an increase in the filling density of MNPs with the increase in the number of FIL cycles. (Figure 5b2, c2, d2).

According to TEM images, the capsules with nanoparticles inside the bulk, obtained using the FIL method, have sharper edges formed by polymer layers. In contrast, capsules with MNPs in the shell (samples 0c1s) have indistinct edges. We can also see individual nanoparticles outside the capsule shell for the sample 0c1s (Figure 5a,a2). Water suspension of all types of capsules is stable in time. Moreover, the layer of MNPs (for sample 0c1s) is further covered with a poly-L-arginine layer and then with a dextran sulfate layer, which gives additional stability and lower probability of MNP desorption.²⁴ Additionally, the comparison of the images in Figure 5 (a, a2) with (b, b2, c, c2, d, d2) shows that samples obtained by LbL (Figure 5a, a2) have a larger diameter than the samples obtained by FIL (Figure 5b, b2, c, c2, d, d2). This can be explained by the following reasoning. Capsules of LbL samples have dense and thick shells.²⁴ During the drying process that accompanies the preparation of the samples for TEM measurements, the shells are ruptured by osmotic pressure and electrostatic repulsion interactions (Coulomb force) between similarly charged MNPs embedded in the polyelectrolyte shell (sample 0c1s). The repulsion force is increased during the drying process because water with high dielectric permittivity evaporates from the shell. Desorption of nanoparticles from the surface of such capsules is caused by osmotic pressure that affects the capsule shell and induces shell damage. Osmotic pressure is proportional to the shell thickness and density. We had previously demonstrated that embedding MNPs in the polymer shell led to increased shell thickness.²⁴ It is confirmed by the results obtained for planar nanocomposite films.^{11,57} The osmotic nature of the capsule shell damage is confirmed by the fact that 0c1s capsules in the dried state (Figure 5a) are larger than the capsules with nanoparticles within the inner volume (Figure 5b, c, and d).

The elemental composition of samples was characterized using SEM with an EDS detector. The EDS spectra of the samples are presented in Figure S1. These measurements are not quantitative and show that iron and oxygen, as elements of magnetite, are present in the samples, which correlates to the observation of MNPs via TEM imaging.

The magnetic moments of the capsules measured by optical tweezers are presented in Table 1 and have the order of

Table 1. Measured and Calculated Characteristics of Submicron Capsules: MNP Number (N_{MNP}) and Mass (M_{MNP}) per Capsule, MNP Volume Fraction ϕ , Mean Interparticle Distance ($\langle r \rangle_v$ for 2c0s, 4c0s, 6c0s and $\langle r \rangle_s$ for 0c1s), Magnetic Moments m_{OT} and m_{VSM} (at $H = 62$ Oe), Relative Scatter of Magnetic Moment Values $\Delta m/m_{\text{OT}}$, SAR, Magnetic Coupling Parameter Γ , and Aggregation Parameter N^*

sample	2c0s	4c0s	6c0s	0c1s
M_{MNP} , pg/caps.	0.13	0.17	0.2	0.09
N_{MNP} , 10^4 /caps.	5.0	6.5	7.6	3.3
ϕ_{MNP} , %	30	39	46	20
MIPD, nm	$\langle r \rangle_v$			$\langle r \rangle_s$
	12	11	10	5
m_{OT} , 10^{-16} A·m ²	3.5 ± 0.3	6.2 ± 0.5	7.2 ± 0.3	4.2 ± 0.4
$\Delta m/m_{\text{OT}}$	0.66	0.61	0.25	0.79
m_{VSM} , 10^{-16} A·m ²	3.1	3.6	7.4	2.6
SAR W/kg	330	290	390	510
Γ	36	114	124	52
N^*	3.6×10^5	3.2×10^{22}	4.8×10^{24}	1.1×10^9

magnitude of 10^{-16} A·m² in the external magnetic field of 62 Oe. In our previous work, we obtained a magnetic moment for three-micron polystyrene beads with magnetite nanograins included (PMPEG-3.0, Kisker Biotech GmbH&Co) using the similar optical tweezers with electromagnets.⁴⁰ In the static external magnetic field with the same strength, the magnetic moment of polystyrene-magnetite beads was $(17.5 \pm 0.8) \times 10^{-15}$ A·m², which exceeds the value of the magnetic moment for the studied capsules because the number of MNPs per bead was much larger. Therefore, the new approach, using an

alternating magnetic field and an oscillating position of the trap, made it possible to determine the magnetic moment of micro-objects more accurately, at least by one order of magnitude.

The results obtained for 2c0s, 4c0s, and 6c0s samples (FIL) show a correlation between the magnitude of the magnetic moment and the concentration of magnetite per capsule. The value of the capsule magnetic moment increases proportionally to the average number of MNPs in the capsule. The sample 0c1s (LbL) exhibited the smallest concentration of magnetite per capsule and was expected to have the smallest magnetic moment. However, the experiment showed that the magnetic moment of capsules for the sample 0c1s was smaller than that for the samples 4c0s and 6c0s, but larger than that for the sample 2c0s. This relates to the fact that MNPs occupy different positions in the capsules in the samples. MNPs for the sample 0c1s are rigidly fixed in the capsule shell and move with the whole capsule, while nanoparticles for samples 2c0s, 4c0s, and 6c0s float within the capsule. The demagnetizing factor of FIL particles is greater than that of LbL particles. Therefore, an increase in the value of the demagnetizing field leads to a decrease in the magnetic moment. The second possible reason that leads to the decrease in the effective magnetic moment for FIL particles obtained in optical tweezers measurements is associated with the redistribution of MNPs inside liquid cores induced by microcapsule magnetic interactions.

The estimation of the average magnetic moment of the particles was also carried out by VSM. Magnetic moment measurements by VSM are referred to as DC measurements because the external magnetic field changes at a low speed. The magnetic field changes at a low frequency of 4 Hz when the magnetic moment is measured using the optical tweezers method. The magnetization dynamic behavior in materials is well studied and described before.^{58,59} There are several mechanisms that lead to differences in magnetic properties in static and dynamic modes. The first mechanism is the occurrence of eddy currents during dynamic magnetization. This mechanism significantly affects the magnitude of the magnetic moment of metal samples in the kilohertz frequency range (magnetite is a dielectric). The second mechanism is the presence of ferromagnetic resonance in the megahertz frequency range. Therefore, from the point of view of magnetic measurements, the optical tweezers method also belongs to the DC type, and both methods are aimed at investigating the static behavior of the magnetic moment in the sample. The hysteresis loop was measured for each sample (Figure 6). All hysteresis loops exhibit superparamagnetic behavior, which is expected for MNPs of this size. The inset of Figure 6 zooms in to compare the data with the results of the optical tweezers measurements in the field of 62 Oe. The accuracy of determining the magnetic moment of the samples under consideration is lower than the accuracy of the optical tweezers measurements. Therefore, the results obtained using magnetometry illustrate the order of magnitude of the magnetic moment per particle, and the correlation between the magnetic moment and the number of nanoparticles per capsule.

In addition to the magnitude of the magnetic moment, initial magnetic susceptibility was determined based on the hysteresis loop. The experimental susceptibility value allows us to estimate the SAR parameter using the method described by Davydov et al. using eq 12.⁴² Our calculation cannot provide the exact value of this parameter because of the use of nonexact approximations for values of anisotropy, the hydrodynamic

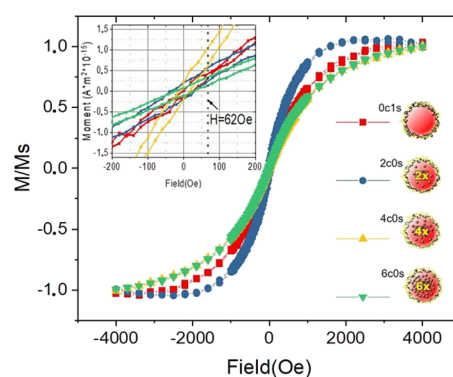


Figure 6. Normalized hysteresis loops for water suspension of various capsules. Sample 0c1s is the nanocomposite shell containing MNPs (the red square) formed using the LbL assembly method. Sample 2c0s is the polymer shell with MNPs encapsulated using FIL with two loading cycles (blue circles), and sample 4c0s corresponds to four cycles (the yellow up-pointing triangle), while sample 6c0s has six cycles (the green down-pointing triangle). The inset illustrates the value of the magnetic moment per particle in the field of 62 Oe.

volume of the microcapsule, and the characteristic time. Despite this, calculations allow us to obtain the order of magnitude of the SAR value and the fact of its change for different types of particles (Table 1). The particles were in a liquid medium ($\eta = 0.001$ Pa·s), and the initial temperature was equal to 23 °C. The external magnetic field was chosen to be 100 Oe with a frequency of 100 kHz, which satisfies Berezovich's criterion.⁶⁰ The constant of magnetic anisotropy is 10^4 J/m³,⁶¹ the characteristic time is 10^{-9} s, and the density of magnetite is 5170 kg/m³.⁶²

The hydrodynamic volume for FIL and LbL capsules was calculated differently. MNPs move freely within the volume of the FIL polymer shell. Therefore, the hydrodynamic volume for microparticles of this type is equal to the volume of nanoparticles that are inside. In the case of LbL microparticles, magnetite is located on the surface of the polymer matrix. This means that nanoparticles are rigidly bound to the polymer and move as a whole. In this case, the hydrodynamic volume of the particle is equal to the volume of the microparticle. Calculation results are shown in Table 1. For samples 2c0s, 4c0s, and 6c0s, the SAR value is approximately the same. However, a change in the architecture of the particle leads to an increase in the Brownian relaxation time, which caused an increase in the calculated parameter. The theoretical estimation of the SAR parameter has shown that this value increases with the incorporation of nanoparticles into the polymer shell (sample 0c1s). The capsules 0c1s are capable of heating by 10–15 °C based on the experimental results, which are presented in previous studies.^{63–65} A slow heating rate to a temperature of 42 °C using an external alternating magnetic field is relevant for hyperthermia. The release of a drug from capsules with MNPs embedded in the shell can be achieved by hyperthermia. The hyperthermic effect can be improved by increasing the MNP loadings of the core and the shell of capsules. The permittivity of the shell can be changed by applying an alternating magnetic field.⁶⁶

Figure 7 illustrates the motion of capsules in a blood vessel under the influence of the external inhomogeneous magnetic field created by a permanent magnet located near the wall of a vessel. The capsules experience the magnetophoretic force and the drag viscous force. The balance of these forces will make

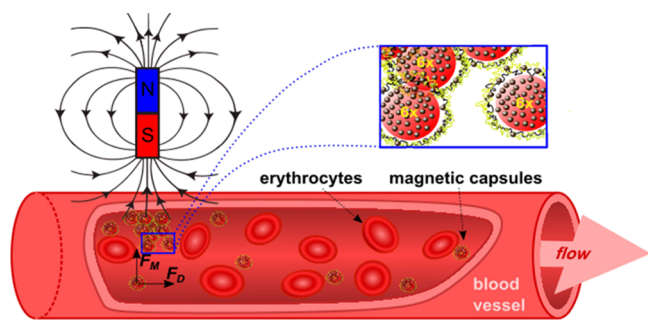


Figure 7. Motion of capsules in a blood vessel in an external inhomogeneous permanent magnetic field. The inset illustrates an enlarged view of the magnetic capsules.

the main contribution to the efficiency of capsule capture by the external magnetic field and its localization in the region of interest, which is especially important for navigable drug delivery.

The magnetophoretic velocity of capsules was calculated as a function of the external magnetic flux density gradient in various environments: blood, plasma, and water. All calculations were performed according to eq 19. The values of the magnetic flux density gradient were taken in the range from 0 to 1 T/mm. The capsule magnetic moment in saturation (Table S1) was calculated from the magnetite magnetization curve (Figure S3) as follows:

$$m_s = M_{\text{MNP}} \cdot |M_s| \quad (20)$$

where M_{MNP} is the MNPs mass per capsule (Table 1) and $|M_s|$ is the mass magnetization of pure magnetite in saturation. The dynamic viscosity coefficient was taken for each environment at a temperature of 37 °C (Table S2). The magnetophoretic velocity of capsules in a Newtonian fluid with a viscosity typical for human blood is shown in Figure 8a. The results for blood plasma and water are presented in Figure S2.

Figure 8b shows that the velocity of samples strongly depends on the amount of encapsulated MNPs; the higher the load, the higher the velocity. The average values of blood flow velocities in cerebral capillaries measured by Ivanov et al. are in the range from 0.5 to 1.5 mm/s, the flow velocity in the majority of muscle capillaries (75%) ranges from 0.6 to 1.5

mm/s, and the velocity above 1.5 mm/s is in 17% of capillaries.⁶⁷ Wolf et al. have shown the mean flow velocity in perimacular capillaries of 3.28 ± 0.45 mm/s in healthy subjects and 2.89 ± 0.57 mm/s in patients with diabetes mellitus.⁶⁸ For the lymphatic capillaries, the median velocities of 0.51 mm/s were shown by Fischer et al.⁶⁹ The magnetophoretic velocities of the particles are comparable to the values of the blood flow velocities in capillaries and the velocities in lymphatic capillaries. Thus, moving these submicron capsules in the magnetic field gradient is a prospective technique for the application in blood capillaries and lymphatic vessels. By comparing the relative scattering of magnetic moment values $\Delta m/m_{\text{OT}}$ (Table 1), one can see that with an increasing amount of MNPs in the samples, the less is the relative scattering of the magnetic moment. The relative scattering for the LbL method for magnetite loading is higher than that for the FIL method.

Table 1 summarizes all experimental data: the number and mass of MNPs per capsule, the volume fraction of MNPs and the MIPD of MNPs inside the capsule, as well as magnetic moments measured using optical tweezers (m_{OT}) and the VSM (m_{VSM}), magnetic parameters of SAR, magnetic coupling parameter Γ , and aggregation parameter N^* . All samples have a diameter of 0.5 ± 0.1 μm , and their concentrations in suspensions used in the studies are $\sim 10^9/\text{mL}$.

The magnetic moment for the first type of capsules loaded with different amounts of MNPs depends on the volume fraction of MNPs and increases with the growing number of MNPs. Both methods, magnetometry and optical tweezers, demonstrate the same trends of the increasing magnetic moment with increasing FIL cycle numbers (Table 1). It was found out that the magnetic moment is determined not only by the amount of magnetite in one capsule but also by the MNP location. Sample 0c1s containing one magnetite layer in the shell (0.09 pg./capsule) shows a higher m_{OT} magnetic moment than sample 2c0s (0.13 pg./capsules) loaded with MNPs using the FIL approach twice. A similar behavior for SAR was observed for samples 0c1s and 2c0s (Table 1).

The magnetic coupling parameter Γ and the aggregation parameter N^* were also calculated (Table 1). Γ is the ratio between the magnetic energy of two magnetized particles and thermal energy. For all samples, the Γ value is significantly

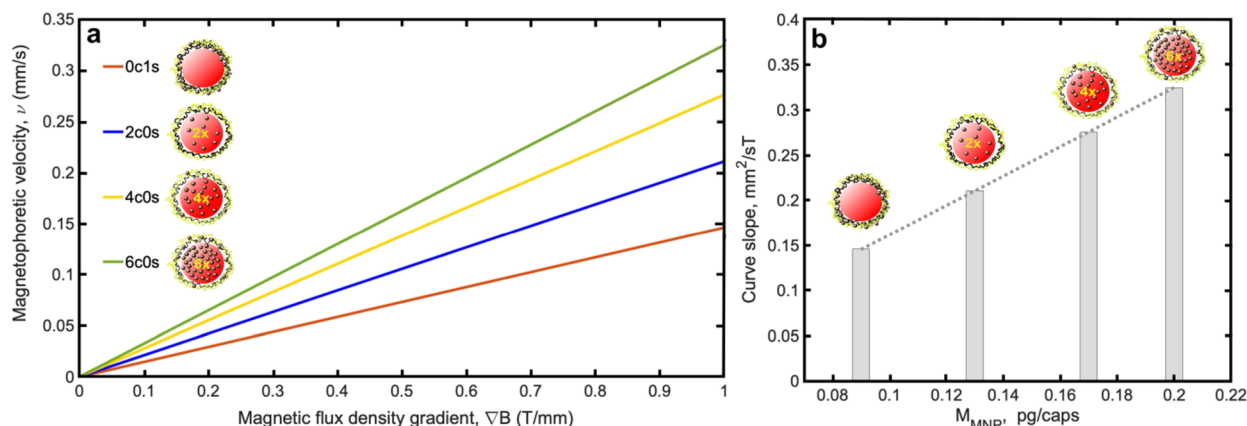


Figure 8. Dependence of the magnetophoretic velocity of capsules in the blood model on the external magnetic flux density gradient for all four samples (a). Sample 0c1s is the nanocomposite shell containing MNPs (red) formed using the LbL assembly method. Sample 2c0s is the polymer shell with MNPs encapsulated using FIL with two loading cycles (blue), and sample 4c0s corresponds to four cycles (yellow), while sample 6c0s has six cycles (green). Dependence of the slope of the magnetophoretic velocity curve on the MNP mass (M_{MNP}) per capsule (b).

higher than the unit value. It means that the magnetic interaction predominates over the thermal one.³¹ The high Γ value leads to an extremely high magnitude of the aggregation parameter N^* for any feasible concentration according to eq 10. The high magnitude of N^* causes the formation of elongated chains from composite shells containing MNPs.³¹ If the aggregation parameter is higher than 10, as it is in our samples, bundles of chains are formed.³¹ Bundle formation has already been demonstrated using optical microscopy.⁸

Therefore, nanocomposite carriers demonstrate the trend to form aggregates under the impact of the magnetic field. The behavior of such types of shells depends on the volume fraction of MNPs and where these MNPs were distributed.

4. CONCLUSIONS

The single submicron polymer/magnetite nanoparticle capsules were synthesized using FIL and LbL assembly methods. Two types of capsules were prepared. The first one is the polymer shell containing the encapsulated MNPs preloaded in the template vaterite core using the FIL method. The amount of MNPs is varied depending on the number of FIL cycles and equals 2, 4, and 6. TEM images of individual capsules confirmed that there are different amounts of MNPs inside polymer shells for samples with different numbers of FIL cycles. The second type of capsules is the nanocomposite shell formed using the LbL assembly method with subsequent absorption of the polymer and MNPs.

The VSM measurements are based on measuring the integral signal from a large number of particles and estimating the average magnetic moment per capsule. This method is less accurate because of a low signal level and the variation in the number of capsules per sample. Measurements using optical tweezers allow for the determination of the magnetic moment of individual capsules. The magnetic moments of more than a dozen capsules of each of the four samples were determined during the measurements. Such a number of measurements makes it possible to obtain some statistics, but nevertheless does not exclude the fact that most of the capsules can have different values of the magnetic moment on average. The relative scattering of the magnetic moment has the lowest value for the submicron capsules with MNPs encapsulated using the FIL method, and the more MNPs are present in capsules, the less is the relative scattering.

The magnetic moment of an individual capsule was measured using the optical tweezers method. The method appeared to be appropriate for measuring the magnetic moment of an individual capsule with an accuracy of 10^{-17} A·m². This allows controlling the magnetic properties of capsules and estimating the force affecting them in the gradient magnetic field in the targeted drug delivery systems.

The results obtained using the optical tweezers method showed that the magnetic moment of microcapsules depends on the type of nanoparticle distribution. The demagnetizing factor of FIL particles is greater than that of LbL particles. The increase in the value of the demagnetizing field leads to a decrease in the magnetic moment.

The SAR parameter was also estimated for various samples. This value slightly varies with the amount of magnetite in an individual capsule, but it depends on the fabrication method. As the MNPs are rigidly bound to the shell, the Néel processes prevail over the Brownian ones and lead to increased heating in an external magnetic field.

The knowledge of the magnetic moment of nanocomposite carriers can be used for calculating the magnetic field and the magnetic field gradient for magnetic separation and target drug delivery navigation. The magnetic coupling parameter Γ was estimated, and it appears to be significantly higher than 1 for all samples. This means that the value of magnetic interaction between two particles is higher than that of thermal energy. Moreover, the magnetic coupling parameter determined the aggregation parameter N^* . The N^* magnitude is higher than 1 for all samples; therefore, the particles formed bundles of chains under the influence of the magnetic field.

The calculated magnetophoretic velocity of particles with the maximum MNP loading using the FIL method is comparable with the velocities of blood flow in different types of capillaries as well as lymphatic vessels. The studied nanocomposite carriers containing MNPs are promising in terms of being applied in the low-gradient magnetic separation of cells and exosomes used in multifunctional drug delivery carriers navigated by the magnetic field gradient monitored by MRI and optoacoustic imaging. The obtained results suggest that capsules made by LbL are better to use for drug delivery because in that case, MNPs are embedded in the shell and do not occupy the place inside of a capsule, which makes more room for the drug to be loaded. In the case of capsules made by FIL, MNPs are loaded into the core, which allows one to achieve maximum concentration of the MNPs inside the shell, and thus, it is better for hyperthermia. Moreover, the remote release approach could be realized through the alternating magnetic field. Additionally, catalytic properties of MNPs presented in the nanocomposite shell can be used for diagnosis and therapy.⁷⁰

■ ASSOCIATED CONTENT

Supporting Information

The Supporting Information is available free of charge at <https://pubs.acs.org/doi/10.1021/acsanm.2c00338>.

EDS spectra of samples 2c0s, 4c0s, and 6c0s; dependence of the magnetophoretic velocity of capsules in water and plasma on the external magnetic flux density gradient; magnetite magnetization curve; calculated saturation magnetic moment of submicron capsules; dynamical viscosity of water, blood, and plasma at 37 °C; and derivation of expressions for the amplitude of capsule oscillations and the magnetic interaction force (PDF)

■ AUTHOR INFORMATION

Corresponding Author

Dmitry A. Gorin — Center for Photonics and Quantum Materials, Skolkovo Institute of Science and Technology, Skolkovo Innovation Center, Moscow 143026, Russia; orcid.org/0000-0001-8760-615X; Email: d.gorin@skoltech.ru

Authors

Evgeny S. Vavaev — Faculty of Physics, Lomonosov Moscow State University, Moscow 119991, Russia; orcid.org/0000-0001-7869-9147

Marina Novoselova — Center for Photonics and Quantum Materials, Skolkovo Institute of Science and Technology, Skolkovo Innovation Center, Moscow 143026, Russia; orcid.org/0000-0001-6268-5058

Nikita M. Shchelkunov – Faculty of Physics, Lomonosov Moscow State University, Moscow 119991, Russia; orcid.org/0000-0002-5330-9031

Sergei German – Center for Photonics and Quantum Materials, Skolkovo Institute of Science and Technology, Skolkovo Innovation Center, Moscow 143026, Russia; Institute of Spectroscopy of the Russian Academy of Sciences, Moscow 108840, Russia; orcid.org/0000-0002-4239-3741

Aleksei S. Komlev – Faculty of Physics, Lomonosov Moscow State University, Moscow 119991, Russia; orcid.org/0000-0003-4319-3781

Maksim D. Mokrousov – Center for Photonics and Quantum Materials, Skolkovo Institute of Science and Technology, Skolkovo Innovation Center, Moscow 143026, Russia; orcid.org/0000-0002-1688-5144

Ivan V. Zelepukin – Shemyakin-Ovchinnikov Institute of Bioorganic Chemistry, Russian Academy of Sciences, Moscow 117997, Russia; orcid.org/0000-0003-0209-2116

Andrey M. Burov – Laboratory of Nanobiotechnology, Institute of Biochemistry and Physiology of Plants and Microorganisms, Saratov 410049, Russia; orcid.org/0000-0002-0469-8392

Boris N. Khlebtsov – Laboratory of Nanobiotechnology, Institute of Biochemistry and Physiology of Plants and Microorganisms, Saratov 410049, Russia; orcid.org/0000-0003-3996-5750

Evgeny V. Lyubin – Faculty of Physics, Lomonosov Moscow State University, Moscow 119991, Russia; orcid.org/0000-0003-2912-5037

Sergey Deyev – Shemyakin-Ovchinnikov Institute of Bioorganic Chemistry, Russian Academy of Sciences, Moscow 117997, Russia

Andrey A. Fedyanin – Faculty of Physics, Lomonosov Moscow State University, Moscow 119991, Russia; orcid.org/0000-0003-4708-6895

Complete contact information is available at: <https://pubs.acs.org/10.1021/acsanm.2c00338>

Author Contributions

The manuscript was written with the contribution of all authors. All authors have given approval to the final version of the manuscript.

Notes

The authors declare no competing financial interest.

ACKNOWLEDGMENTS

Marina Novoselova, Sergei German, and Dmitry A. Gorin were partly supported by the Russian Foundation for Basic Research (18-290846, synthesis of magnetite nanoparticles, vaterite particles, and fabrication of capsules), Andrey A. Fedyanin was supported by the Russian Science Foundation (20-12-00371, optical tweezers measurements). TEM images were obtained at the Symbiosis Center for the Collective Use of Research Equipment in the Field of Physical–Chemical Biology and Nanobiotechnology, IBPPM RAS. The work by Sergei German was supported by the Russian Foundation for Basic Research, project No. 19-33-60089. Aleksei S. Komlev acknowledges support from the Russian Ministry of Science and Education grant No. 075-15-2021-1353. This research was conducted under the MSU Interdisciplinary Scientific and Educational

School “Photonic and Quantum technologies. Digital medicine.”

REFERENCES

- (1) Wilhelm, S.; Tavares, A. J.; Dai, Q.; Ohta, S.; Audet, J.; Dvorak, H. F.; Chan, W. C. W. Analysis of Nanoparticle Delivery to Tumours. *Nat. Rev. Mater.* **2016**, *1*, 1–12.
- (2) Stetciura, I. Y.; Yashchenok, A.; Masic, A.; Lyubin, E. V.; Inozemtseva, O. A.; Drozdova, M. G.; Markvichova, E. A.; Khlebtsov, B. N.; Fedyanin, A. A.; Sukhorukov, G. B.; Gorin, D. A.; Volodkin, D. V. Composite SERS-Based Satellites Navigated by Optical Tweezers for Single Cell Analysis. *Analyst* **2015**, *140*, 4981–4986.
- (3) Wu, M.; Ouyang, Y.; Wang, Z.; Zhang, R.; Huang, P.; Chen, C.; Li, H.; Li, P.; Quinn, D.; Dao, M.; Suresh, S.; Sadovsky, Y.; Huang, T. J. Isolation of Exosomes from Whole Blood by Integrating Acoustics and Microfluidics. *Proc. Natl. Acad. Sci. U. S. A.* **2020**, *117*, 28525.
- (4) Voronin, D. V.; Sindeeva, O. A.; Kurochkin, M. A.; Mayorova, O.; Fedosov, I. V.; Semyachkina-Glushkovskaya, O.; Gorin, D. A.; Tuchin, V. V.; Sukhorukov, G. B. In Vitro and in Vivo Visualization and Trapping of Fluorescent Magnetic Microcapsules in a Bloodstream. *ACS Appl. Mater. Interfaces* **2017**, *9*, 6885–6893.
- (5) Ozcelik, A.; Rufo, J.; Guo, F.; Gu, Y.; Li, P.; Lata, J.; Huang, T. J. Acoustic Tweezers for the Life Sciences. *Nat. Methods* **2018**, *15*, 1021–1028.
- (6) Felfoul, O.; Mohammadi, M.; Taherkhani, S.; de Lanauze, D.; Zhong Xu, Y.; Loghin, D.; Essa, S.; Jancik, S.; Houle, D.; Lafleur, M.; Gaboury, L.; Tabrizian, M.; Kaou, N.; Atkin, M.; Vuong, T.; Batist, G.; Beauchemin, N.; Radzioch, D.; Martel, S. Magneto-Aerotactic Bacteria Deliver Drug-Containing Nanoliposomes to Tumour Hypoxic Regions. *Nat. Nanotechnol.* **2016**, *11*, 941–947.
- (7) Schuerle, S.; Soleimany, A. P.; Yeh, T.; Anand, G. M.; Häberli, M.; Fleming, H. E.; Mirkhani, N.; Qiu, F.; Hauert, S.; Wang, X.; Nelson, B. J.; Bhatia, S. N. Synthetic and Living Micropropellers for Convection-Enhanced Nanoparticle Transport. *Sci. Adv.* **2019**, *5*, No. eaav4803.
- (8) Novoselova, M. V.; German, S. V.; Abakumova, T. O.; Perevoschikov, S. V.; Sergeeva, O. V.; Nesterchuk, M. V.; Efimova, O. I.; Petrov, K. S.; Chernyshev, V. S.; Zatssepina, T. S.; Gorin, D. A. Multifunctional Nanostructured Drug Delivery Carriers for Cancer Therapy: Multimodal Imaging and Ultrasound-Induced Drug Release. *Colloids Surf. B Biointerface* **2021**, *200*, No. 111576.
- (9) Kolesnikova, T. A.; Akchurin, G. G.; Portnov, S. A.; Khomutov, G. B.; Akchurin, G. G.; Naumova, O. G.; Sukhorukov, G. B.; Gorin, D. A. Visualization of Magnetic Microcapsules in Liquid by Optical Coherent Tomography and Control of Their Arrangement via External Magnetic Field. *Laser Phys. Lett.* **2012**, *9*, 643–648.
- (10) Mokrousov, M. D.; Novoselova, M. V.; Nolan, J.; Harrington, W.; Rudakovskaya, P.; Bratashov, D. N.; Galanzha, E. I.; Fuenzalida-Werner, J. P.; Yakimov, B. P.; Nazarikov, G.; Drachev, V. P.; Shirshin, E. A.; Ntziachristos, V.; Stiel, A. C.; Zharov, V. P.; Gorin, D. A. Amplification of Photoacoustic Effect in Bimodal Polymer Particles by Self-Quenching of Indocyanine Green. *Biomed. Opt. Express* **2019**, *10*, 4775.
- (11) Gorin, D. A.; Portnov, S. A.; Inozemtseva, O. A.; Luklinska, Z.; Yashchenok, A. M.; Pavlov, A. M.; Skirtach, A. G.; Möhwald, H.; Sukhorukov, G. B. Magnetic/Gold Nanoparticle Functionalized Biocompatible Microcapsules with Sensitivity to Laser Irradiation. *Phys. Chem. Chem. Phys.* **2008**, *10*, 6899–6905.
- (12) Vlasova, K. Y.; Vishwasrao, H.; Abakumov, M. A.; Golovin, D. Y.; Gribanovsky, S. L.; Zhigachev, A. O.; Poloznikov, A.; Majouga, A. G.; Golovin, Y. I.; Sokolsky-Papkov, M.; Klyachko, N. L.; Kabanov, A. V. Enzyme Release from Polyion Complex by Extremely Low Frequency Magnetic Field. *Sci. Rep.* **2020**, *10*, 4745.
- (13) Golovin, Y. I.; Gribanovsky, S. L.; Golovin, D. Y.; Klyachko, N. L.; Majouga, A. G.; Master, A. M.; Sokolsky, M.; Kabanov, A. V. Towards Nanomedicines of the Future: Remote Magneto-Mechanical Actuation of Nanomedicines by Alternating Magnetic Fields. *J. Controlled Release* **2015**, *219*, 43–60.

- (14) Korolovych, V. F.; Grishina, O. A.; Inozemtseva, O. A.; Selifonov, A. V.; Bratashov, D. N.; Suchkov, S. G.; Bulavin, L. A.; Glukhova, O. E.; Sukhorukov, G. B.; Gorin, D. A. Impact of High-Frequency Ultrasound on Nanocomposite Microcapsules: In Silico and in Situ Visualization. *Phys. Chem. Chem. Phys.* **2016**, *18*, 2389–2397.
- (15) German, S. V.; Novoselova, M. V.; Bratashov, D. N.; Demina, P. A.; Atkin, V. S.; Voronin, D. V.; Khlebtsov, B. N.; Parakhonskiy, B. V.; Sukhorukov, G. B.; Gorin, D. A. High-Efficiency Freezing-Induced Loading of Inorganic Nanoparticles and Proteins into Micron- and Submicron-Sized Porous Particles. *Sci. Rep.* **2018**, *8*, 17763.
- (16) German, S. V.; Navolokin, N. A.; Kuznetsova, N. R.; Zuev, V. V.; Inozemtseva, O. A.; Anis'kov, A. A.; Volkova, E. K.; Bucharskaya, A. B.; Maslyakova, G. N.; Fakhrullin, R. F.; Terentyuk, G. S.; Vodovozova, E. L.; Gorin, D. A. Liposomes Loaded with Hydrophilic Magnetic Nanoparticles: Preparation and Application as Contrast Agents for Magnetic Resonance Imaging. *Colloids Surf. B Biointerface* **2015**, *135*, 109–115.
- (17) Barmin, R. A.; Rudakovskaya, P. G.; Gusliakova, O. I.; Sindeeva, O. A.; Prikhodzhenko, E. S.; Maksimova, E. A.; Obukhova, E. N.; Chernyshev, V. S.; Khlebtsov, B. N.; Solovov, A. A.; Sukhorukov, G. B.; Gorin, D. A. Air-Filled Bubbles Stabilized by Gold Nanoparticle/Photodynamic Dye Hybrid Structures for Theranostics. *Nanomaterials* **2021**, *11*, 415.
- (18) Nikitin, A. A.; Shchetinin, I. V.; Tabachkova, N. Y.; Soldatov, M. A.; Soldatov, A. V.; Sviridenkova, N. V.; Beloglazkina, E. K.; Savchenko, A. G.; Fedorova, N. D.; Abakumov, M. A.; Majouga, A. G. Synthesis of Iron Oxide Nanoclusters by Thermal Decomposition. *Langmuir* **2018**, *34*, 4640–4650.
- (19) Sheparovych, R.; Sahoo, Y.; Motornov, M.; Wang, S.; Luo, H.; Prasad, P. N.; Sokolov, I.; Minko, S. Polyelectrolyte Stabilized Nanowires from Fe₃O₄ Nanoparticles via Magnetic Field Induced Self-Assembly. *Chem. Mater.* **2006**, *18*, 591–593.
- (20) Mohan, P.; Rapoport, N. Doxorubicin as a Molecular Nanotheranostic Agent: Effect of Doxorubicin Encapsulation in Micelles or Nanoemulsions on the Ultrasound-Mediated Intracellular Delivery and Nuclear Trafficking. *Mol. Pharmaceutics* **2010**, *7*, 1959–1973.
- (21) Karukstis, K. K.; Thompson, E. H. Z.; Whiles, J. A.; Rosenfeld, R. J. Deciphering the Fluorescence Signature of Daunomycin and Doxorubicin. *Biophys. Chem.* **1998**, *73*, 249–263.
- (22) Decher, G. Fuzzy Nanoassemblies: Toward Layered Polymeric Multicomposites. *Science* **1997**, *277*, 1232–1237.
- (23) Sukhorukov, G. B.; Donath, E.; Lichtenfeld, H.; Knippel, E.; Knippel, M.; Budde, A.; Möhwal, H. Layer-by-Layer Self Assembly of Polyelectrolytes on Colloidal Particles. *Colloids Surf. A Physicochem. Eng. Asp.* **1998**, *137*, 253–266.
- (24) Andreeva, D. V.; Gorin, D. A.; Shchukin, D. G.; Sukhorukov, G. B. Magnetic Microcapsules with Low Permeable Polypyrrole Skin Layer. *Macromol. Rapid Commun.* **2006**, *27*, 931–936.
- (25) German, S. V.; Bratashov, D. N.; Navolokin, N. A.; Kozlova, A. A.; Lomova, M. V.; Novoselova, M. V.; Burilova, E. A.; Zhev, V. V.; Khlebtsov, B. N.; Bucharskaya, A. B.; Terentyuk, G. S.; Amirov, R. R.; Maslyakova, G. N.; Sukhorukov, G. B.; Gorin, D. A. In Vitro and in Vivo MRI Visualization of Nanocomposite Biodegradable Microcapsules with Tunable Contrast. *Phys. Chem. Chem. Phys.* **2016**, *18*, 32238–32246.
- (26) Kozlova, A. A.; German, S. V.; Atkin, V. S.; Zhev, V. V.; Astle, M. A.; Bratashov, D. N.; Svenskaya, Y. I.; Gorin, D. A. Magnetic Composite Submicron Carriers with Structure-Dependent MRI Contrast. *Inorganics* **2020**, *8*, 11.
- (27) Hu, B.; Han, L.; Ma, R.; Phillips, G. O.; Nishinari, K.; Fang, Y. All-Natural Food-Grade Hydrophilic-Hydrophobic Core-Shell Micro-particles: Facile Fabrication Based on Gel-Network-Restricted Antisolvent Method. *ACS Appl. Mater. Interfaces* **2019**, *11*, 11936–11946.
- (28) Díez-Pascual, A. M.; Díez-Vicente, A. L. Magnetic Fe₃O₄@poly(Propylene Fumarate-Co-Ethylene Glycol) Core-Shell Biomaterials. *RSC Adv.* **2017**, *7*, 10221–10234.
- (29) Yammine, E.; Souaid, E.; Youssef, S.; Abboud, M.; Mornet, S.; Nakhli, M.; Duguet, E. Particles with Magnetic Patches: Synthesis, Morphology Control, and Assembly. *Part. Part. Syst. Charact.* **2020**, *37*, No. 2000111.
- (30) Timonen, J. V. I.; Grzybowski, B. A. Tweezing of Magnetic and Non-Magnetic Objects with Magnetic Fields. *Adv. Mater.* **2017**, *29*, No. 1603516.
- (31) Leong, S. S.; Ahmad, Z.; Low, S. C.; Camacho, J.; Faraudo, J.; Lim, J. K. Unified View of Magnetic Nanoparticle Separation under Magnetophoresis. *Langmuir* **2020**, *36*, 8033–8055.
- (32) Dobashi, T.; Yeh, F. J.; Ying, Q.; Ichikawa, K.; Chu, B. An Experimental Investigation on the Structure of Microcapsules. *Langmuir* **1995**, *11*, 4278–4282.
- (33) Chu, B.; Liu, T. Characterization of Nanoparticles by Scattering Techniques. *J. Nanopart. Res.* **2000**, *2*, 29–41.
- (34) Kolovskaya, O. S.; Zamay, T. N.; Zamay, G. S.; Babkin, V. A.; Medvedeva, E. N.; Neverova, N. A.; Kirichenko, A. K.; Zamay, S. S.; Lapin, I. N.; Morozov, E. V.; Sokolov, A. E.; Narodov, A. A.; Fedorov, D. G.; Tomilin, F. N.; Zabluda, V. N.; Alekhina, Y.; Lukyanenko, K. A.; Glazyrin, Y. E.; Svetlichnyi, V. A.; Berezovski, M. V.; Kichkailo, A. S. Aptamer-Conjugated Superparamagnetic Ferriarabinogalactan Nanoparticles for Targeted Magnetodynamic Therapy of Cancer. *Cancers* **2020**, *12*, 216.
- (35) Andrade, V. M.; Vivas, R. J. C.; Pedro, S. S.; Tedesco, J. C. G.; Rossi, A. L.; Coelho, A. A.; Rocco, D. L.; Reis, M. S. Magnetic and Magnetocaloric Properties of La_{0.6}Ca_{0.4}MnO₃ Tunable by Particle Size and Dimensionality. *Acta Mater.* **2016**, *102*, 49–55.
- (36) Ashkin, A. Acceleration and Trapping of Particles by Radiation Pressure. *Phys. Rev. Lett.* **1970**, *24*, 156–159.
- (37) Neuman, K. C.; Block, S. M. Optical Trapping. *Rev. Sci. Instrum.* **2004**, *75*, 2787–2809.
- (38) Shilkin, D. A.; Lyubin, E. V.; Soboleva, I. V.; Fedyanin, A. A. Direct Measurements of Forces Induced by Bloch Surface Waves in a One-Dimensional Photonic Crystal. *Opt. Lett.* **2015**, *40*, 4883.
- (39) Skryabina, M. N.; Lyubin, E. V.; Khokhlova, M. D.; Fedyanin, A. A. Probing of Pair Interaction of Magnetic Microparticles with Optical Tweezers. *JETP Lett.* **2012**, *95*, 560–564.
- (40) Romodina, M. N.; Khokhlova, M. D.; Lyubin, E. V.; Fedyanin, A. A. Direct Measurements of Magnetic Interaction-Induced Cross-Correlations of Two Microparticles in Brownian Motion. *Sci. Rep.* **2015**, *5*, 10491.
- (41) Kumar, C. S. S. R.; Mohammad, F. Magnetic Nanomaterials for Hyperthermia-Based Therapy and Controlled Drug Delivery. *Adv. Drug Delivery Rev.* **2011**, *63*, 789–808.
- (42) Davydov, A. S.; Belousov, A. V.; Krusanov, G. A.; Kolyvanova, M. A.; Kovalev, B. B.; Komlev, A. S.; Krivoshapkin, P. V.; Morozov, V. N.; Zverev, V. I. Promising Magnetic Nanoradiosensitizers for Combination of Tumor Hyperthermia and X-Ray Therapy: Theoretical Calculation. *J. Appl. Phys.* **2021**, *129*, No. 033902.
- (43) Wang, S. C.; Neoh, K. G.; Kang, E. T.; Pack, D. W.; Leckband, D. E. Synthesis and Functionalization of Polypyrrole-Fe₃O₄ Nanoparticles for Applications in Biomedicine. *J. Mater. Chem.* **2007**, *17*, 3354–3362.
- (44) Biase, J. N.; Whitehead, E. D.; Miller, F.; Hoffman, S. Unilateral Unitary Inflatable Penile Prosthesis to Correct Impaired Tumescence and Severe Penile Deformity Resulting from Traumatic Rupture of 1 Corpus Cavernosum. *J. Urol.* **1994**, *152*, 2098–2100.
- (45) Pchelina, D. I.; Medvetskaya, I. Y.; Chistyakova, N. I.; Rusakov, V. S.; Sedykh, V. D.; Alekhina, Y. A. Mössbauer and Magnetic Studies of Doped Lanthanum Manganite La_{1-x}CaxMnO₃ (x = 0.05, 0.10, 0.20): II. Stoichiometric Composition and Phase Segregation. *J. Surf. Investig.* **2019**, *13*, 462–468.
- (46) Pimentel, B.; Caraballo-Vivas, R. J.; Checca, N. R.; Zverev, V. I.; Salakhova, R. T.; Makarova, L. A.; Pyatakov, A. P.; Perov, N. S.; Tishin, A. M.; Shtil, A. A.; Rossi, A. L.; Reis, M. S. Threshold Heating Temperature for Magnetic Hyperthermia: Controlling the Heat Exchange with the Blocking Temperature of Magnetic Nanoparticles. *J. Solid State Chem.* **2017**, *2018*, 34–38.

- (47) Dan'kov, S. Y.; Tishin, A. M.; Pecharsky, V. K.; Gschneidner, K. A. Magnetic Phase Transitions and the Magnetothermal Properties of Gadolinium. *Phys. Rev. B* **1998**, *57*, 3478–3490.
- (48) Nauman, M.; Alnasir, M. H.; Hamayun, M. A.; Wang, Y.; Shatruck, M.; Manzoor, S. Size-Dependent Magnetic and Magnetothermal Properties of Gadolinium Silicide Nanoparticles. *RSC Adv.* **2020**, *10*, 28383–28389.
- (49) Pavlov, A. M.; Gabriel, S. A.; Sukhorukov, G. B.; Gould, D. J. Improved and Targeted Delivery of Bioactive Molecules to Cells with Magnetic Layer-by-Layer Assembled Microcapsules. *Nanoscale* **2015**, *7*, 9686–9693.
- (50) Carregal-Romero, S.; Guardia, P.; Yu, X.; Hartmann, R.; Pellegrino, T.; Parak, W. J. Magnetically Triggered Release of Molecular Cargo from Iron Oxide Nanoparticle Loaded Microcapsules. *Nanoscale* **2015**, *7*, 570–576.
- (51) Luo, D.; Poston, R. N.; Gould, D. J.; Sukhorukov, G. B. Magnetically Targetable Microcapsules Display Subtle Changes in Permeability and Drug Release in Response to a Biologically Compatible Low Frequency Alternating Magnetic Field. *Mater. Sci. Eng. C* **2019**, *94*, 647–655.
- (52) Novoselova, M. V.; German, S. V.; Sindeeva, O. A.; Kulikov, O. A.; Novoselova, O. V.; Brodovskaya, E. P.; Ageev, V. P.; Zharkov, M. N.; Pyataev, N. A.; Sukhorukov, G. B.; Gorin, D. A. Submicron-Sized Nanocomposite Magnetic-Sensitive Carriers: Controllable Organ Distribution and Biological Effects. *Polymers* **2019**, *11*, 1082.
- (53) Lyubin, E. V.; Khokhlova, M. D.; Skryabina, M. N.; Fedyanin, A. A. Cellular Viscoelasticity Probed by Active Rheology in Optical Tweezers. *J. Biomed. Opt.* **2012**, *17*, No. 101510.
- (54) Romodina, M. N.; Lyubin, E. V.; Fedyanin, A. A. Detection of Brownian Torque in a Magnetically-Driven Rotating Microsystem. *Sci. Rep.* **2016**, *6*, No. 21212.
- (55) Salem, S. F.; Tuchin, V. V. Magnetic Particle Trapping in a Branched Blood Vessel in the Presence of Magnetic Field. *J. Biomed. Photonics Eng.* **2020**, *6*, No. 040302.
- (56) Gleich, B.; Hellwig, N.; Bridell, H.; Jurgons, R.; Seliger, C.; Alexiou, C.; Wolf, B.; Weyh, T. Design and Evaluation of Magnetic Fields for Nanoparticle Drug Targeting in Cancer. *IEEE Trans. Nanotechnol.* **2007**, *6*, 164–170.
- (57) Grigoriev, D.; Gorin, D.; Sukhorukov, G. B.; Yashchenok, A.; Maltseva, E.; Möhwald, H. Polyelectrolyte/Magnetite Nanoparticle Multilayers: Preparation and Structure Characterization. *Langmuir* **2007**, *23*, 12388–12396.
- (58) Tikadumi, S. Physics of Ferromagnetism. Magnetic Properties of a Substance. *M.:Mir* **1983**, 420.
- (59) *The Science of Hysteresis: Physical Modeling, Micromagnetics, and Magnetization Dynamics*; Bertotti, G., Mayergoyz, I., Eds.; Gulf Professional Publishing, 2006, Vol II.
- (60) Hergt, R.; Dutz, S. Magnetic Particle Hyperthermia-Biophysical Limitations of a Visionary Tumour Therapy. *J. Magn. Magn. Mater.* **2007**, *311*, 187–192.
- (61) Mamiya, H.; Fukumoto, H.; Cuya Huaman, J. L.; Suzuki, K.; Miyamura, H.; Balachandran, J. Estimation of Magnetic Anisotropy of Individual Magnetite Nanoparticles for Magnetic Hyperthermia. *ACS Nano* **2020**, *14*, 8421–8432.
- (62) van der Zee, J. Heating the Patient: A Promising Approach? *Ann. Oncol.* **2002**, *13*, 1173–1184.
- (63) Elkhova, T. M.; Yakushechkina, A. K.; Semisalova, A. S.; Gun'ko, Y. K.; Spichkin, Y. I.; Pyatakov, A. P.; Kamilov, K. I.; Perov, N. S.; Tishin, A. M. Heating of Zn-Substituted Manganese Ferrite Magnetic Nanoparticles in Alternating Magnetic Field. *Solid State Phenom.* **2015**, 233–234, 761–765.
- (64) Salakhova, R. T.; Vylegzhanin, A. G.; Kashtanov, E. A.; Zverev, V. I.; Müller, R.; De Sena Pereira, F. D.; Parfenov, V. A.; Mironov, V. A.; Kritskaya, E. A.; Pyatakov, A. P.; Markov, V. K.; Malyshev, A. Y.; Kamilov, K. I.; Tishin, A. M. Frequency Dependence of Magnetothermal Properties for Magnetic Fluid and Magnetically Functionalized Implants. *EPJ Web Conf.* **2018**, *185*, 1–4.
- (65) Ferreira, M. C.; Pimentel, B.; Andrade, V.; Zverev, V.; Gimaev, R. R.; Pomorov, A. S.; Pyatakov, A.; Alekhina, Y.; Komlev, A.; Makarova, L.; Perov, N.; Reis, M. S. Understanding the Dependence of Nanoparticles Magnetothermal Properties on Their Size for Hyperthermia Applications: A Case Study for La-Sr Manganites. *Nanomaterials* **2021**, *11*, 1826.
- (66) Timin, A. S.; Gao, H.; Voronin, D. V.; Gorin, D. A.; Sukhorukov, G. B. Inorganic/Organic Multilayer Capsule Composition for Improved Functionality and External Triggering. *Adv. Mater. Interfaces* **2017**, *4*, No. 1600338.
- (67) Ivanov, K. P.; Kalinina, M. K.; Levkovich, Y. I. Blood Flow Velocity in Capillaries of Brain and Muscles and Its Physiological Significance. *Microvasc. Res.* **1981**, *22*, 143–155.
- (68) Wolf, S.; Arend, O.; Toonen, H.; Bertram, B.; Jung, F.; Reim, M. Retinal Capillary Blood Flow Measurement with a Scanning Laser Ophthalmoscope Preliminary Results. *Ophthalmology* **1991**, *98*, 996–1000.
- (69) Fischer, M.; Franzeck, U. K.; Herrig, I.; Costanzo, U.; Wen, S.; Schiesser, M.; Hoffmann, U.; Bollinger, A. Flow Velocity of Single Lymphatic Capillaries in Human Skin. *Am. J. Physiol.* **1996**, *270*, H358.
- (70) Mujtaba, J.; Liu, J.; Dey, K. K.; Li, T.; Chakraborty, R.; Xu, K.; Makarov, D.; Barmin, R. A.; Gorin, D. A.; Tolstoy, V. P.; Huang, G.; Solovov, A. A.; Mei, Y. Micro-Bio-Chemo-Mechanical-Systems: Micromotors, Microfluidics, and Nanozymes for Biomedical Applications. *Adv. Mater.* **2021**, *33*, No. e2007465.